Terahertz near-field nanoscopy based on detectorless laser feedback interferometry under different feedback regimes

Cite as: APL Photon. 6, 061302 (2021); doi: 10.1063/5.0048099
Submitted: 19 February 2021 • Accepted: 7 June 2021 •
Published Online: 23 June 2021

Eva A. A. Pogna,[1] Carlo Silvestri,[2] Lorenzo L. Columbo,[2] Massimo Brambilla,[3] Gaetano Scamarcio,[3] and Miriam S. Vitiello[1,a)]

AFFILIATIONS

[1] NEST, CNR-Istituto Nanoscienze and Scuola Normale Superiore, Piazza San Silvestro 12, 56127 Pisa, Italy
[2] Dipartimento di Elettronica e Telecomunicazioni Politecnico di Torino, Corso Duca degli Abruzzi 24, 10129 Torino, Italy
[3] Dipartimento Interateneo di Fisica, Università degli Studi di Bari Aldo Moro e Politecnico di Bari, via Amendola 173, I70126 Bari, Italy

[a)] **Author to whom correspondence should be addressed:** miriam.vitiello@sns.it

ABSTRACT

Near-field imaging techniques, at terahertz frequencies (1–10 THz), conventionally rely on bulky laser sources and detectors. Here, we employ a semiconductor heterostructure laser as a THz source and, simultaneously, as a phase-sensitive detector, exploiting optical feedback interferometry combined with scattering near-field nanoscopy. We analyze the amplitude and phase sensitivity of the proposed technique as a function of the laser driving current and of the feedback attenuation, discussing the operational conditions ideal to optimize the nano-imaging contrast and the phase sensitivity. As a targeted nanomaterial, we exploit a thin (39 nm) flake of $Bi_2Te_{2.2}Se_{0.8}$, a topological insulator having infrared active optical phonon modes. The self-mixing interference fringes are analyzed within the Lang–Kobayashi formalism to rationalize the observed variations as a function of Acket's parameter C in the full range of weak feedback ($C < 1$).

Near-field nanoscopy,[1–5] relying on the measurement of scattered light from nanostructures and nanomaterials, represents a powerful method for inspecting the optical properties of nanosized samples with sub-diffraction spatial resolution and for accessing regimes of strong-light matter interaction by exploiting the electromagnetic (e.m.) field enhancement into volumes smaller than the optical wavelength.[6–10] Extending near-field nanoscopy into the terahertz (THz) frequency range, where the characteristic e.m. field has wavelength λ ranging between 30 μm and 300 μm, provides a great potential in this respect, and it is often prescribed to resolve spatial dis-homogeneities of the optical response at the sub-micron scale.[11–24] However, one of the major challenges for THz near-field nanoscopy is the availability of reliable (>10 mW average power) THz sources, sensitive detectors (noise equivalent powers NEP $< 10^{-12}$ W/Hz$^{1/2}$), and probes with high scattering efficiency[25] to sense backscattered optical powers, which are usually a fraction of 10^{-9}–10^{-4} of the laser output.

In near-field nanoscopy, the standard experimental strategy to measure the near-field scattering is based on the operation of the near-field probe in tapping mode, at frequencies of the order of hundreds of kHz, to modulate the near-field component of the scattered intensity. Accordingly, the employed photodetectors need to have high sensitivity (NEP $< 10^{-12}$ W/Hz$^{1/2}$) and simultaneously operate on timescales ($<\mu$s) fast enough to follow the signal modulation induced by the tapping. Standard THz detectors employed in THz nanoscopy include room-temperature Schottky diodes and Golay cells or hot-electron bolometers. The slow time response of thermal detectors (pyrometers and Si bolometers) conversely hinders their use for high resolution near-field experiments.

Recently, an alternative compact detection scheme,[18,22] relying on the intracavity re-injection of the radiation emitted from a THz quantum cascade laser (QCL),[26] through self-mixing interferometry (SMI),[27–31] has been demonstrated. The nonlinear interference of the beam reflected from a nanostructure with the optical field

inside the laser cavity depends on the relative phase difference of the two superimposed e.m. fields and causes perturbation of all lasing parameters, including the lasing frequency and the threshold gain, which, in turn, results into a variation of the laser voltage under constant current operation. The latter process is inherently fast since the maximum response speed to optical feedback is determined by the frequency of the relaxation oscillations in the laser. In the case of THz-QCLs, the lifetime of the upper state of the lasing transition is limited by elastic and inelastic scattering mechanisms to 5–10 ps,[26,32] enabling, in principle, response frequencies of the order of 100 GHz.

A wide variety of applications of self-mixing interferometry in diode lasers[30,33] and QCLs[18,22,34–38] has been demonstrated including metrology,[30,33] sensing,[34] and imaging.[16,34–38] The laser is typically operated slightly above the lasing threshold[30] and for interferometric applications, the amplitude of the re-injected field is kept low in order to work in the limit of the so-called very weak feedback regime in which the SMI fringe line shape is simply sinusoidal.[22,39,40]

Here, we employ scattering near-field optical microscopy (s-SNOM) in a detectorless configuration at THz frequencies to investigate the near-field SMI signal as a function of the feedback amplitude and the operation current of the employed QCL source and to identify the preferable operating conditions [giving high signal-to-noise ratio (SNR), high speed, and large optical contrast] for near-field nano-imaging applications. By exploiting the intrinsic stability of THz-QCL to large feedback intensity,[40] we demonstrate that even by driving the QCL source at currents much larger than the lasing threshold, we can achieve high-contrast and low noise crucial ingredients for high resolution and fast nano-imaging.

By modeling the THz-QCL in the presence of the optical feedback through the formalism set by the Lang–Kobayashi equations,[39] we discuss the observed dependence of the self-mixing signal on the laser feedback and the laser driving current in terms of modifications of the optical feedback Acket's parameter *C*. We then explore the dependence of the phase sensitivity of SMI on the feedback intensity and QCL currents and show that the first-order Taylor expansion of the solution of the Lang–Kobayashi equations,[39] for laser frequencies around the free running one, provides a good approximation of the signal amplitude and phase in the so-called weak feedback regime where the SMI fringes are asymmetric and cannot be described by an analytical function. Based on that the optical sampling of SMI fringes for phase determination can be strongly reduced. Finally, we validate the proposed method by applying the SMI nanoscopy to a topological insulating bismuth compound, which is endowed with resonant excitations in the THz range.

These results are of paramount importance for the development of coherent THz near-field nanoscopy systems based on THz-QCL sources and, more generally, pave the way for exploring novel domains for a more efficient detection based on the self-mixing process.

The experimental setup employed for THz near-field nanoscopy is shown in Fig. 1(a). It exploits a set of THz-QCLs fabricated with a single plasmon waveguide,[26] operating in continuous wave (CW) at the driving current I_{QCL}, with output frequencies of either $\omega = 2.0$ THz or $\omega = 2.7$ THz and peak powers at 15 K of P = 5 mW and P = 4.2 mW, respectively. The QCL beam is collimated with a 90° off-axis parabolic (OAP) gold mirror with 50 mm focal length, and it is coupled to a commercial scattering scanning near-field microscope (s-SNOM) from Neaspec. The THz beam is focused on a metallic AFM tip with a 60° incident angle relative to the tip axis by a 25 mm OAP.

In the experiments reported in this work, we have employed the same tip. The strength of the near-field signal strongly depends on the tip geometry. The latter determines the field enhancement at the tip apex and how efficiently the near-field is converted into the far-field to be detected through self-mixing interferometry, i.e., the net dipole moment associated with the tip. For experiments that do not require sub-100 nm spatial resolution, higher sensitivity can be attained by choosing tips of larger radius. Recent numerical simulations[25] indeed predict that by increasing the radius from 25 to 750 nm, the s-SNOM signal strength is expected to increase by one order of magnitude at the expense of only a factor four reduction in the spatial resolution. We use PtIr coated AFM tips (Rocky Mountain Nanotechnology) with 20 nm apex radius and an 80 μm-long tip to exploit the enhanced scattering efficiency at THz frequencies of tens of μm s long cantilever tips.[41]

A portion of the THz field, which is backscattered by the tip, re-injected into the laser cavity and detected through the induced variations of the laser voltage ΔV due to a self-mixing effect.[22] The tip works in tapping mode with frequency Ω = 70–110 kHz such that the signal includes oscillating near-field components $\Delta V = \Sigma_n \Delta V_n e^{i\Omega n}$, which can be isolated from the background due to the far-field illumination of the tip shaft and the sample by lock-in detection at the harmonics $\Omega_n = n\Omega$ of the tapping frequency with n = 1, . . ., 5 demodulation order. The tapping motion modulates the amplitude of the backscattered field, which is re-injected into the laser cavity without varying the optical path length. The incident power and the feedback intensity are controlled by inserting a variable attenuator (THz attenuator set from Microtech instruments) with transmittance T = 10%, 30%, and 60% in the optical path, along segments of the collimated propagating beam.

To detect the SMI fringes, we vary the relative phase between the incident and backscattered fields by changing the length of the external cavity formed by the tip and the output facet of the THz-QCL with an optical delay line consisting of two 45° flat mirrors mounted on a linear translation stage (Physik Instrument model M-413) with 0.16 μm resolution. This later corresponds to a minimum variation of the cavity length L = 0.32 μm, which allows for a fine sampling of the SMI fringes that are characterized by $\lambda/2$ periodicity equal to ~37–150 μm in the range of 1–4 THz.

We first investigate the imaging capability of the experimental setup with a THz-QCL emitting at 2.7 THz by raster scanning a 75 nm thick gold film evaporated on a Si undoped substrate with a 300 nm SiO_2 top layer, whose topography map is reported in Fig. 1(b). The tip is brought in close proximity to the sample, which is scanned by moving the sample holder with a three-axes piezomotor. The signal intensity is expected to increase with the tapping amplitude,[44] which is kept constantly equal to 280 nm for the measurements on the gold marker. The near-field maps collected at different demodulation orders n = 2, . . ., 5 are shown in Fig. 1(c); the maps are acquired by keeping fixed the cavity length at a value chosen to maximize the SMI signal. The scattered signal amplitude reflects the dielectric properties of the sample and increases at the gold marker, as expected, based on the higher reflectivity[43,44] of gold at 2.7 THz, compared to that of the silica/silicon substrate.

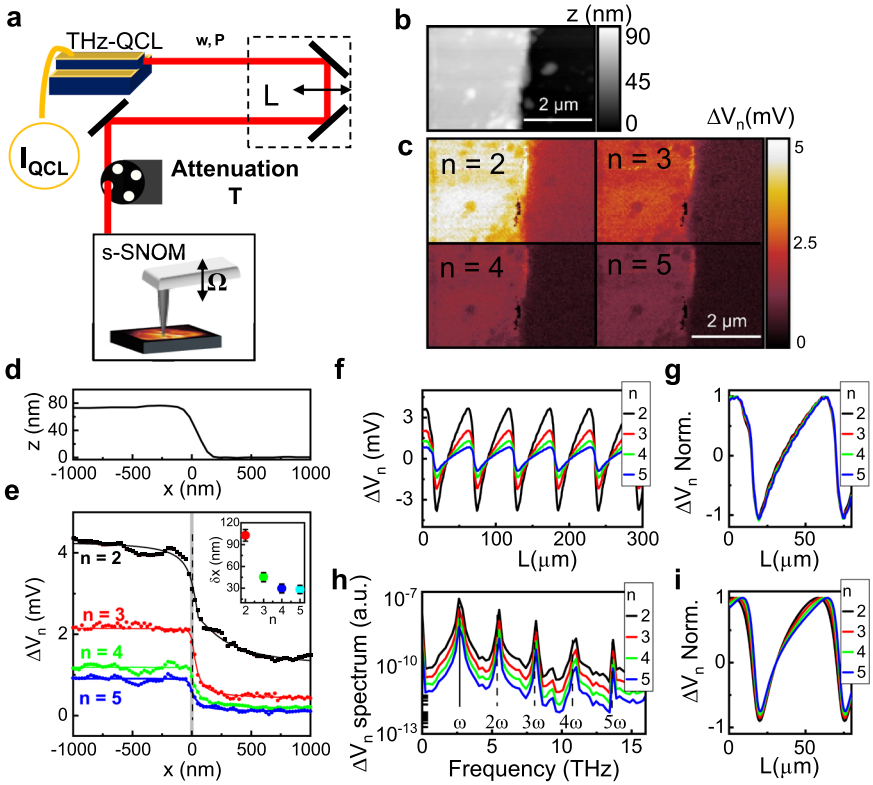

FIG. 1. (a) Sketch of the experimental setup for THz near-field nanoscopy employing a THz-QCL lasing at frequency ω, coupled to an s-SNOM from Neaspec equipped with an AFM tip operating in tapping mode at frequency Ω. The operational parameters that define the setup performance include the laser output power P, the driving THz-QCL current I_{QCL}, the optical feedback intensity controlled with a variable attenuators of transmission T, and the optical path length changed by L with an optical delay line. (b) Topography map of an Au film (leftmost side) deposited on an undoped Si substrate with a 300 nm SiO_2 top layer. (c) Maps of the near-field SMI signal ΔV_n demodulated at the n_{th} harmonics of the tapping frequency Ω acquired with ω = 2.7 THz, T = 100%, I_{QCL} = 690 mA, and L = 50 μm. (d) and (e) Spatial resolution estimation from the analysis of (d) topography and (e) near-field SMI signal ΔV_n (solid dots) line scans, taken across the Au/Si interface in the maps (b) and (c), together with (solid colored lines) the best fit to the asymmetric step function[42] of widths δx at the Au side shown in the inset as a function of the demodulation order n. (f) Near-field SMI signal ΔV_n from gold as a function of the cavity length variations L at different demodulation orders *n*. (g) Normalized near-field SMI signal ΔV_n from (f). (h) Fourier transform spectrum of the ΔV_n fringes in (f) at demodulation orders *n* showing peaks at the laser frequency ω and its harmonics.[43] (i) Simulated normalized SMI fringes at the second, third, fourth, and fifth harmonics, obtained by solving LK equations to find the combination of C and α parameters (C = 0.5 and α = 0.5) that best describes the experimental fringes of panel (g).

The line scans extracted from the maps in Fig. 1(c), integrating along the direction orthogonal to the gold–substrate interface, are reported in Fig. 1(e). We estimate the spatial resolution of the setup by analyzing the signal step-like variation at the gold/substrate interface with the empirically found asymmetric fit function from Ref. 42, which takes into account that the different light confinement at the metal and the substrate sides gives rise to non-point symmetric line profiles. The step in the topography at the boundary complicates a reliable determination of the spatial resolution due to tip–sample convolution, which would require the analysis of the signal variation at topography-free sharp boundaries.[42,44,45] The derivative of the fitting function, which corresponds to the line spread function of our imaging system, is a piecewise Lorentzian with width δx at the metal side. As expected, due to the tip-sharpening effect,[14] both the signal amplitude and δx decrease with the demodulation order *n* [see Fig. 1(e)]. Remarkably, the width δx = 28 nm at the n = 5 demodulation order would correspond to a spatial resolution of λ/4000, significantly exceeding the limit posed by diffraction (~λ/2 = 55.5 μm). The near-field nature of the signal is reflected by the strong monotonic decrease of signal amplitude as the tip–sample distance is increased (see the supplementary material, Fig. S1). The third demodulation order is chosen in the following discussion as a good compromise between signal intensity and far-field background suppression.

The SMI fringes, acquired at a fixed position at the gold marker, are reported in Fig. 1(g) as a function of *L*, which is used to tune the phase difference between the laser field and the retro-injected field. The asymmetric line shape indicates that, despite the fact that the tip is scattering only a reduced portion of the incident radiation, the laser does not exhibit a response typical of a very weak feedback regime, with its characteristic sinusoidal dependence on *L*. The Fourier spectra in Fig. 1(h) describe the spatial periodicity of the SMI fringes (λ/2) that translate into the fundamental and the harmonics of the QCL emission frequency. The presence of higher harmonics is directly related with the characteristic asymmetric line shape of SMI fringes for field feedback values of the order of 10^{-4}–10^{-3}.

Interestingly, we observe that for high demodulation orders n > 1, the fringes have the same normalized line shape. The first demodulation order instead has a distinct line shape and distinct phase frequency spectrum that can be attributed to residual contributions from the far-field background. To analyze the self-mixing fringes, we apply the Lang–Kobayashi model[39] with the feedback strength parameter describing the fraction of the backscattered light that efficiently couples to the lasing mode, which depends on sample reflectivity. The best agreement [Fig. 1(h)] is obtained with Acket's characteristic parameter C = 0.5 and Henry's linewidth enhancement factor α = 0.5, which is in good agreement with reported values for a similar QCL in the THz range.[46]

With the aim of identifying the regime providing the best compromise of the SNR, phase sensitivity, and scan speed, we investigated the dependence of the near-field signal on two key experimental parameters: the QCL driving current I_{QCL} and the feedback intensity. We performed two sets of experiments employing two different THz-QCLs emitting at 2.0 and 2.7 THz. The scattering efficiency of the AFM tip is strongly wavelength dependent[41] and a reduction of the scattered field is indeed expected for an increasing photon energy.

Figures 2(a) and 2(b) show a selection of near-field self-mixing maps measured at the third demodulation order ΔV_3 for increasing I_{QCL}, acquired at the two probing frequencies.

To quantify the variation in the near-field signal amplitude, we extract 5 μm-long line profiles [Figs. 2(c) and 2(d)], along the perpendicular to the marker/substrate interface, by averaging the maps of Figs. 2(a) and 2(b), vertically, over a 100 nm range. The ΔV_3

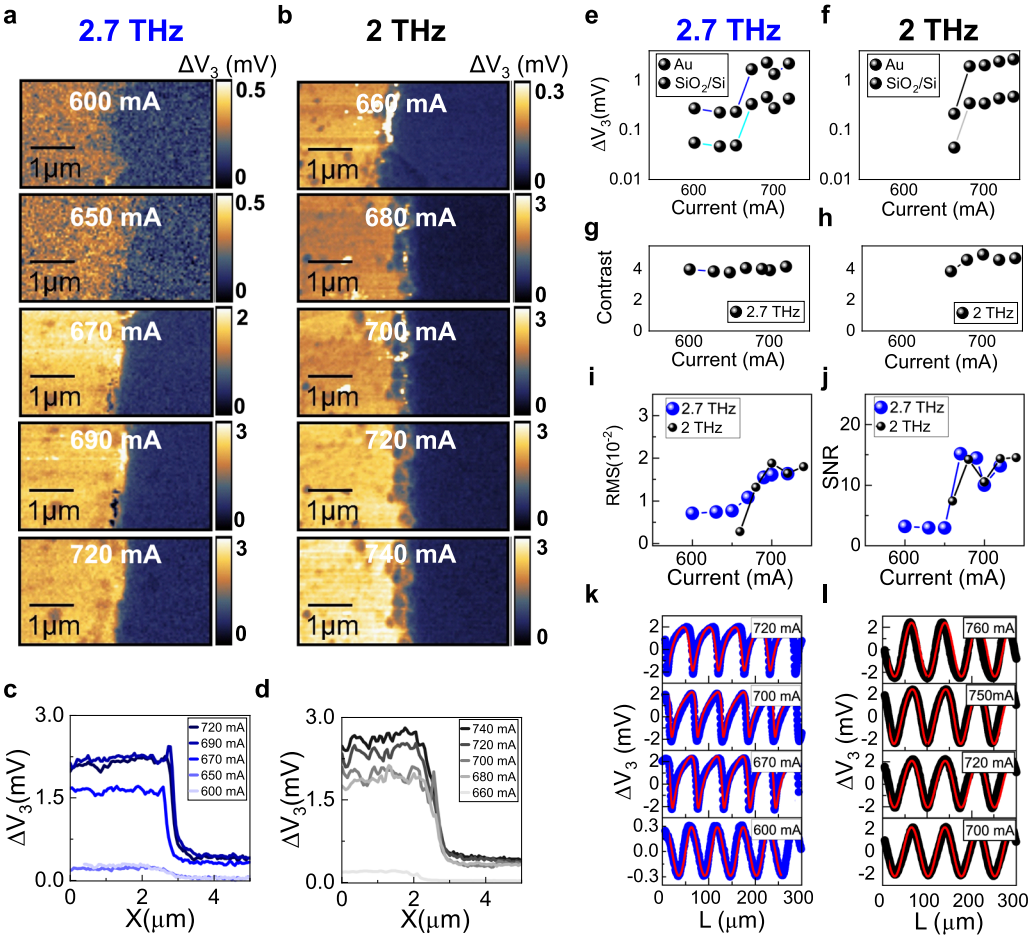

FIG. 2. (a) and (b) Selection of near-field ΔV_3 maps of the Au marker at fixed L = 50 μm, corresponding to a fringe maximum, for increasing I_{QCL} from top to bottom and QCL frequency (a) 2.7 THz and (b) 2.0 THz. (c) and (d) Line profiles extracted from panels (a) and (b) across the Au–SiO_2/Si interface at (c) 2.7 THz and (d) 2.0 THz for different I_{QCL}. (e) and (f) ΔV_3 signal amplitude evaluated from the line scans in panels (c) and (d) averaging on 1 μm range at (e) 2.7 THz and (f) 2.0 THz on (blue and black dots) Au and the (ciano and gray dots) SiO_2/Si substrate. (g) and (h) Contrast evaluated as the ratio between the signal on Au and the signal on the SiO_2/Si substrate at (g) 2.7 THz and (h) 2.0 THz. (i) Root-mean-square (rms) of the maps evaluated on 20 × 50 pixels^2 sections of the ΔV_3 maps in (a) and (b) as a function of I_{QCL} at (blue dots) 2.7 THz and (black dots) 2.0 THz. (j) Signal-to-noise ratio (SNR) evaluated dividing the average signal ΔV_3 from panels (e) and (f) by the noise from panel (i) as a function of I_{QCL}. (k) and (l) SMI fringes at [blue dots, (k)] 2.7 THz and [black dots, (l)] 2.0 THz at different I_{QCL} together with the simulated curve (red solid lines) for α = 0.5 and *C* parameter from bottom up equal to C = {0.05, 0.5, 0.5, 0.63, 0.5} at 2.7 THz and C = {0.01, 0.05, 0.2, 0.5} at 2.0 THz.

signal increases above the laser threshold on both the Au and SiO_2/Si substrate sides, with an enhancement factor of 7.5 above 660 mA at 2.7 THz [Fig. 2(e)] and of 9.1 above 670 mA at 2.0 THz [Fig. 2(f)]. The change in the signal amplitude reflects a mode hopping[47] unveiled by Fourier transforming the self-mixing fringes acquired for a 30 mm-long *L*-scan (see the supplementary material, Fig. S3). Above I_{QCL} = 650 mA (at 2.7 THz) and I_{QCL} = 660 mA (at 2.0 THz), both lasers operate in the regime of C ≥ 0.5, and the self-mixing signal remains stable and constant with I_{QCL}, as expected, given that the ratio between the output and the reinjected field amplitudes is not changing.

We estimate the ΔV_3 amplitude on gold and on the substrate in Figs. 2(e) and 2(f) by averaging along the 1 μm-long portion of the line scans of Figs. 2(c) and 2(d), where the topography is flat. Despite the variation of the absolute signal with increasing the current I_{QCL}, the ratio between the signal measured on gold and that measured on the substrate remains constant with a maximum 5% variation at 2.0 THz. The image contrast is indeed an intrinsic property related to the dielectric constants of the probed materials. Within the framework of analytic[48,49] and numerical models[50–52] of the tip–sample interaction, the image contrast measured with THz s-SNOM allows for quantitative determination of the complex-valued dielectric permittivity, which, in turn, contains information on the material's vibrational modes[22] and on the charge-carrier density beyond its Drude-like response.[53–55] We measure a constant contrast of about 4, at both pumping frequencies, as a consequence of the flat spectral response of gold and SiO_2/Si in the probed frequency range.

Since the image contrast is preserved while varying I_{QCL}, we can analyze the noise in the maps. The increase in the signal is accompanied by an increase in the root-mean-square (rms) [Fig. 2(i)], evaluated on bi-dimensional regions of 20 × 20 pixels^2 in the maps shown in Figs. 2(a) and 2(b). However, the SNR in Fig. 2(f) is optimized at high I_{QCL} values due to the relatively higher improvement in terms of the signal amplitude. Based only on the SNR, the high-current high-power working condition seems preferable.

A very-good quantitative agreement with the experiments is obtained for calculated fringes with the α = 0.5 and *C* parameter in the range of 0.05–0.63 for 2.7 THz and 0.01–0.2 for 2.0 THz (see the supplementary material). The very weak feedback regime is reached when the fringes have a sinusoidal dependence on *L*, corresponding to *C* < 0.1. At the threshold current, the fringes are sinusoidal at 2.7 and 2.0 THz corresponding to C < 0.1. For higher currents, we have to use higher values of the C parameter (C > 0.1) to describe the fringes of the 2.7 THz laser due to the asymmetry of the asymmetry of their lineshape.

We then consider the effect of the feedback intensity on the near-field self-mixing signal by keeping constant the driving current I_{QCL}, above the threshold, while varying the filter transmission T, as shown in Figs. 3(a)–3(d). Higher T transmission corresponds to higher feedback intensity, and T = 100% is achieved by removing the filter wheel from the optical path. The signal amplitude on gold and the substrate is first evaluated by extracting the line scans shown in Figs. 3(c) and 3(d) and then by averaging along portions of flat topography as we have done for the analysis of the self-mixing signal as a function of I_{QCL} discussed before. The average signal in Figs. 3(e) and 3(f), at both 2.0 and 2.7 THz, drops with the reduction in the feedback intensity, following a linear dependence. However, the contrast between gold and the substrate in Figs. 3(g) and 3(h) remains constant within a 1% variation, as expected.

In close analogy to the aforementioned dependence on I_{QCL}, the SNR follows the correlation of the signal amplitude with feedback intensity such that despite the increase in the rms [see Fig. 3(i)], the SNR is larger in the high-feedback regime [see Fig. 3(j)].

The effect of attenuation on the fringes line shape is similar to that observed when decreasing I_{QCL}, as reported in Figs. 3(k) and 3(l) where the experimental results are superimposed to the numerical ones. The SMI fringes become gradually more symmetric by reducing the feedback intensity and sinusoidal interference fringes appear in the very weak regime, attained for T = 30% at both 2.0 and 2.7 THz. Accordingly, the C parameters that better describe the experimental data decrease linearly with the filter transmission from C = 0.4 to C = 0.03 (see the supplementary material). The linear dependence of C on the attenuator transmission is expected since with the attenuator, we are varying the ratio between the output power and the re-injected field amplitude.

To explore the dependence of phase sensitivity on the feedback intensity, we investigate the near-field response of a thin (39 nm) flake of $Bi_2Te_{2.2}Se_{0.8}$. This topological insulator material has infrared active optical phonon modes[56] in the range of 1.6–2.8 THz. In this frequency range, phase variations of the near-field scattered field are expected, as induced by the interaction of the impinging light with these optical phonons. The phase variation can be detected as a shift of the SMI fringes as a function of *L*, as previously shown in CsBr.[22]

Figures 4(a)–4(c) show the topography of the $Bi_2Te_{2.2}Se_{0.8}$ flake together with the corresponding near-field SMI maps, acquired at 2.0 THz while driving the QCL at I_{QCL} = 700 mA, keeping *L* fixed and using a tapping amplitude of 130 nm. We compare the maps of the third-order SMI signal acquired under two different feedback levels, obtained by using an attenuator transmission T = 100% and T = 30%. In both the cases, we observe that the near-field SMI signal is enhanced at the flake with respect to the undoped silicon/silica substrate, with signal peaked at the flake's edges, signature of edge resonances of phonon-polariton modes.[57]

To retrieve the phase of the SMI signal from the flake, we move on the sample along a line orthogonal to the flake/substrate interface, following the path indicated in Fig. 4(b), with 30 nm steps, acquiring SMI fringes as a function of L at each position X on the sample. The fringe maps as a function of L and X are reported in Figs. 4(d)–4(f) for three different attenuator transmission T = 10%, 30%, 100%. The fringes change the line shape with the feedback attenuation, as previously observed for gold, becoming increasingly asymmetric with increasing T, as shown in Fig. 4(g), by the comparison of the fringes at X = 150 nm for T = 30% and 100%.

In the very weak feedback limit, reached at T = 30%, the voltage change at the QCL terminals can be described[3] by the relation $\Delta V_3 = s_3 \cos(\omega_0 \frac{2L}{c} - \varphi_3)$, where ω_0 is the unperturbed laser frequency, *L* is the external cavity length, *c* is the light speed in vacuum, and s_3 and φ_3 are the amplitude and phase of the SMI fringes, respectively. The phase and amplitude can be thus retrieved by a fitting algorithm, based on the least squares method, using a sinusoidal fitting function. The outcome of the fitting procedure is shown in Figs. 4(h) and 4(i), as obtained by fixing ω_0 = 2.0 THz and setting the amplitude s_3 and the phase φ_3 as fitting variables. A finite phase shift is observed for the field scattered by the flake indicating the

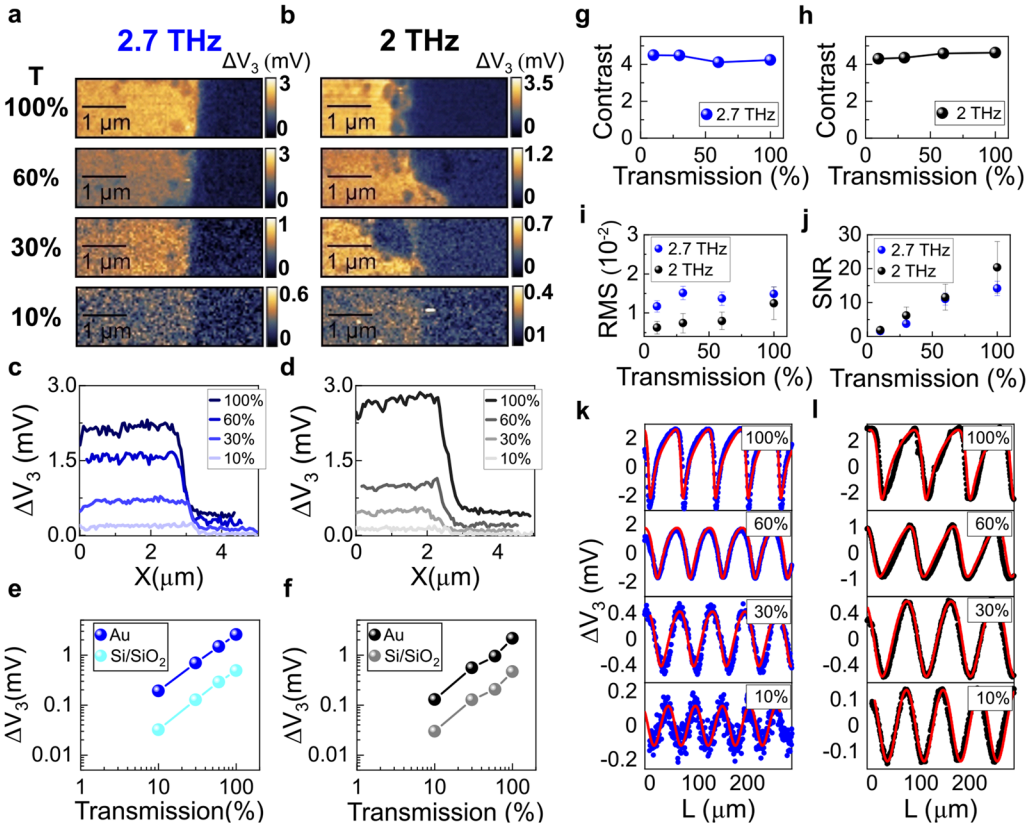

FIG. 3. (a) and (b) Near-field ΔV_3 maps of the Au marker at fixed L = 50 μm, corresponding to a fringe maximum, for increasing attenuation from top to bottom achieved with a filter of transmission T = 100%, 60%, 30%, 10% at QCL frequency (a) 2.7 THz and (b) 2.0 THz. (c) and (d) Line profiles extracted from panels (a) and (b) across the Au–SiO_2/Si interface at (c) 2.7 THz and (d) 2.0 THz for different filter transmission T = {10%, 30%, 60%, 100%}. (e) and (f) Average signal on the substrate and on gold, retrieved along a 1 μm-long portion of the line scans in panels (c) and (d). (g) and (h) Signal contrast as a function of the attenuator transmission at (g) 2.7 THz and (h) 2.0 THz obtained dividing the signal from gold with that of the substrate taken from panels (e) and (f). (i) Statistical analysis of the images with rms evaluated in a 20 × 20 pixels^2 area of maps in panels (a) and (b) as a function of attenuator transmission. (j) Signal-to-noise ratio (SNR) evaluated from panels (e), (f) and (l) as a function of attenuator transmission. (k) and (l) SM fringes as a function of L, measured with attenuators of different transmission increasing from the lower to upper panels [blue dots, (k)] at 2.7 THz and [black dots, (l)] 2.0 THz together with the simulated curve (red solid lines) calculated with $\alpha = 0.5$ and C parameters increasing linearly with the attenuator transmission as shown in the supplementary material.

activation of phonon-polariton modes, predicted for Bi_2Se_3 in this frequency range.[58]

For higher feedback strength, i.e., moving from the very weak to the weak regime, a sizable deviation from the sinusoidal dependence is observed as shown by the SMI fringes acquired with attenuator transmission T = 100% in Fig. 4(g). In the latter case, the scattering amplitude and phase retrieval becomes more complex since, to account for the experimental line shape of the SMI fringes, additional components at harmonics of ω_0 should be considered [Fig. 1(h)]. We observe that the amplitude and phase retrieved from a sinusoidal fit in Figs. 4(h) and 4(i) (colored open dots) show a similar trend along the sample for all three datasets, including the case T = 100% (open dots).

Each of the analyzed fringes consists of about 150 points in the cavity length. We integrate the signal for 10 ms per point for a total of ~2 s per fringe at a fixed position on the sample to be compared with the 13.5 s acquisition time per spectrum achieved with hyperspectral near-field imaging based on THz time domain spectroscopy (TDS)[59] and with 0.3 s with nano-FTIR holography.[60] In order to fulfill the antialiasing theorem, the sampling rate must not exceed the Nyquist rate, which is equal to two times the highest frequency of the periodic signal. Accordingly, the presence of high frequency components in the high-feedback regime imposes a finer sampling of the SMI fringes. This later implies, in turn, a longer acquisition time per pixel, which would be especially detrimental for measurements that require high spectral resolution and larger sampling of the fringes, as is the case for those based on multimode sources[61] for hyperspectral imaging.

In order to identify a faster routine for retrieving the amplitude and phase of the SMI fringes, valid even in the presence of non-sinusoidal fringes, we consider the first-order Taylor expansion of the perturbed laser frequency (with feedback), around the unperturbed frequency, and use the expansion in the expression of the contact voltage $\Delta V(L)$ as a function of the cavity length L in

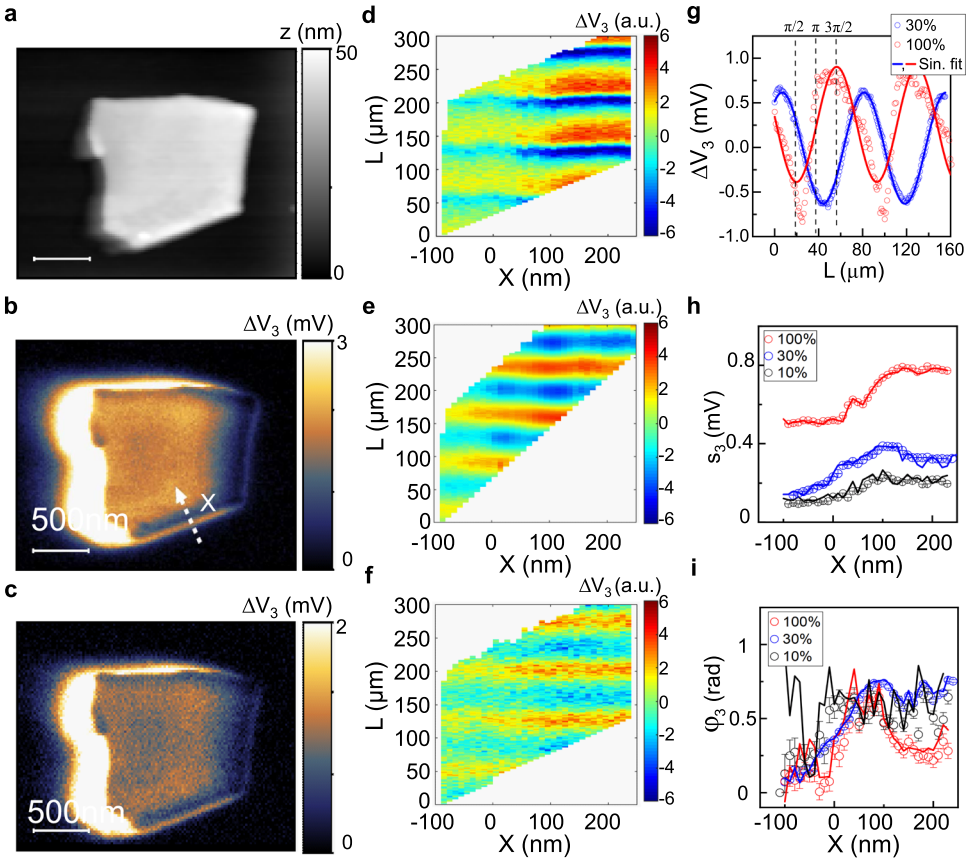

FIG. 4. (a) Topography of a 39 nm thick flake of $Bi_2Te_{2.2}Se_{0.8}$ measured by AFM. (b) and (c) Near-field ΔV_3 maps of the flake at fixed $L = 50\ \mu$m, corresponding to a fringe maximum, measured (b) without the attenuator, i.e., T = 100%, and (c) with the attenuator T = 30%. (d)–(f) SMI fringes acquired on the white dashed arrow in (b) as a function of the position X on the line crossing the substrate–flake interface and of L. The fringes are measured (d) without the attenuator, (e) with T = 30%, and [(f)] with T = 10%. The fringe maps look tilted because of a finite backlash in the translation stage controlling the external cavity length. (g) SMI fringes on $Bi_2Te_{2.2}Se_{0.8}$ for two different values of attenuator transmission (blue open dots) T = 30% and (red open dots) T = 100% obtained by cutting panels (d) and (e) at X = 150 nm, together with the best fit with the sinusoidal fitting function (colored solid lines). (h) Amplitude s_3 and (i) phase φ_3 of the signal as a function of the position X on the dashed line in panel (b) as extracted from the sinusoidal fit (open dots) with the attenuator of variable transmission (black open dots) T = 10%, (blue open dots) 30%, and (red open dots) 100%, together with the corresponding results of the amplitude and phase determination using Eqs. (14) and (15) of the supplementary material as colored solid lines.

the weak regime (see the supplementary material). In the approximated formulas, given by Eqs. (15) and (16) of the supplementary material, the signal amplitude s_3 and its phase φ_3 are evaluated from the values of the signal third harmonic $\Delta V_3(L)$ at four different values of L, reciprocally phase shifted by $\pi/2$, corresponding to a displacement of $L = \lambda/8$. The amplitude and phase profiles extracted with the approximated method in Figs. 4(h) and 4(i) (colored solid lines) show quantitative agreement with those determined from the sinusoidal fit (colored open dots). The deviation observed for φ_3 extracted at the highest attenuation (T = 10%) for X < 0 at the substrate side may be attributed to the low SNR (<2) of the data, affecting more the analysis with the approximated formula that is based on only four points in L and has been introduced to describe the signal at higher feedback levels. At the flake side, where the signal increases, the agreement with the sinusoidal fits and with the estimations for T > 10% is recovered. Accordingly, we conclude that the sinusoidal fit provides a reliable determination of s_3 and φ_3 also in the presence of a higher feedback level, i.e., in the weak feedback regime.

Moreover, we got the evidence that a faster routine relying on the measurement of only four values of the signal $\Delta V_3(L)$, as described above, can be exploited to extract the same type of information (amplitude and phase) with a higher degree of accuracy, being valid even in the presence of non-sinusoidal fringes.

In conclusion, we exploit self-mixing interferometry under different feedback regimes to study a detectorless THz near-field optical microscope built on THz-QCLs. Its operational performances are then investigated in terms of the image contrast and SNR as a function of the THz-QCL driving current and the feedback intensity. The observed signals are interpreted within the Lang–Kobayashi formalism under operational conditions, ranging from the very weak ($C < 0.1$) to the weak ($0.1 < C < 1$) feedback regimes. The best imaging conditions in terms of the SNR are obtained in the high feedback regime. Despite the more-complex non-sinusoidal line shape of the

self-mixing fringes, the latter leads to optimized performances in terms of the SNR. A first-order approximated method is used to evaluate the self-mixing signal phase and amplitude even for non-sinusoidal fringes, allowing for an efficient, in terms of scan speed, and reliable image reconstruction.

The supplementary material describes the approach curves, the emission spectrum, the evolution of Acket's parameter C as a function of the current and the feedback, and the signal increase with tapping amplitude. It also presents the Lang–Kobayashi model for SD s-SNOM and the first-order reconstruction of the scattering coefficient harmonics.

This work was supported by the European Research Council through the ERC Consolidator Grant (681379) SPRINT. M.S.V. acknowledges partial support from the second half of the Balzan Prize 2016 in applied photonics delivered to Federico Capasso.

DATA AVAILABILITY

The data that support the findings of this study are available from the corresponding author upon reasonable request.

REFERENCES

[1] E. Betzig, J. K. Trautman, T. D. Harris, J. S. Weiner, and R. L. Kostelak, "Breaking the diffraction barrier: Optical microscopy on a nanometric scale," Science **251**, 1468–1470 (1991).
[2] F. Keilmann, "Surface-polariton propagation for scanning near-field optical microscopy application," J. Microsc. **194**, 567–570 (1999).
[3] R. Hillenbrand, T. Taubner, and F. Keilmann, "Phonon-enhanced light–matter interaction at the nanometre scale," Nature **418**, 159–162 (2002).
[4] A. Bouhelier, J. Renger, M. R. Beversluis, and L. Novotny, "Plasmon-coupled tip-enhanced near-field optical microscopy," J. Microsc. **210**, 220–224 (2003).
[5] F. Keilmann and R. Hillenbrand, "Near-field microscopy by elastic light scattering from a tip," Philos. Trans. R. Soc. London, Ser. A **362**, 787–805 (2004).
[6] A. J. Huber *et al.*, "Near-field imaging of mid-infrared surface phonon polariton propagation," Appl. Phys. Lett. **87**, 081103 (2005).
[7] D. N. Basov, M. M. Fogler, and F. J. García de Abajo, "Polaritons in van der Waals materials," Science **354**, 6309 (2016).
[8] T. Low *et al.*, "Polaritons in layered two-dimensional materials," Nat. Mater. **16**, 182–194 (2017).
[9] M. A. Huber *et al.*, "Femtosecond photo-switching of interface polaritons in black phosphorus heterostructures," Nat. Nanotechnol. **12**, 207–211 (2017).
[10] W. Ma *et al.*, "In-plane anisotropic and ultra-low-loss polaritons in a natural van der Waals crystal," Nature **562**, 557–562 (2018).
[11] A. J. Huber, F. Keilmann, J. Wittborn, J. Aizpurua, and R. Hillenbrand, "Terahertz near-field nanoscopy of mobile carriers in single semiconductor nanodevices," Nano Lett. **8**, 3766–3770 (2008).
[12] H.-T. Chen, R. Kersting, and G. C. Cho, "Terahertz imaging with nanometer resolution," Appl. Phys. Lett. **83**, 3009–3011 (2003).
[13] H.-T. Chen, S. Kraatz, G. C. Cho, and R. Kersting, "Identification of a resonant imaging process in apertureless near-field microscopy," Phys. Rev. Lett. **93**, 267401 (2004).
[14] H.-G. von Ribbeck, M. Brehm, D. W. van der Weide, S. Winnerl, O. Drachenko, M. Helm, and F. Keilmann, "Spectroscopic THz near-field microscope," Opt. Express **16**, 3430–3438 (2008).
[15] A. J. L. Adam, "Review of near-field terahertz measurement methods and their applications," J. Infrared, Millimeter, Terahertz Waves **32**, 976–1019 (2011).
[16] K. Moon, H. Park, J. Kim, Y. Do, S. Lee, G. Lee, H. Kang, and H. Han, "Subsurface nanoimaging by broadband terahertz pulse near-field microscopy," Nano Lett. **15**, 549–552 (2015).
[17] F. Kuschewski, H.-G. von Ribbeck, J. Döring, S. Winnerl, L. M. Eng, and S. C. Kehr, "Narrow-band near-field nanoscopy in the spectral range from 1.3 to 8.5 THz," Appl. Phys. Lett. **108**, 113102 (2016).
[18] P. Dean, O. Mitrofanov, J. Keeley, I. Kundu, L. Li, E. H. Linfield, and A. Giles Davies, "Apertureless near-field terahertz imaging using the self-mixing effect in a quantum cascade laser," Appl. Phys. Lett. **108**, 091113 (2016).
[19] C. Liewald, S. Mastel, J. Hesler, A. J. Huber, R. Hillenbrand, and F. Keilmann, "All-electronic terahertz nanoscopy," Optica **5**, 159–163 (2018).
[20] P. Klarskov, H. Kim, V. L. Colvin, and D. M. Mittleman, "Nanoscale laser terahertz emission microscopy," ACS Photonics **4**, 2676–2680 (2017).
[21] R. Degl'Innocenti, R. Wallis, B. Wei, L. Xiao, S. J. Kindness, O. Mitrofanov, P. Braeuninger-Weimer, S. Hofmann, H. E. Beere, and D. A. Ritchie, "Terahertz nanoscopy of plasmonic resonances with a quantum cascade laser," ACS Photonics **4**, 2150–2157 (2017).
[22] M. C. Giordano, S. Mastel, C. Liewald, L. L. Columbo, M. Brambilla, L. Viti, A. Politano, K. Zhang, L. Li, A. G. Davies, E. H. Linfield, R. Hillenbrand, F. Keilmann, G. Scamarcio, and M. S. Vitiello, "Phase-resolved terahertz self-detection near-field microscopy," Opt. Express **26**, 18423–18435 (2018).
[23] J. Zhang, X. Chen, S. Mills, T. Ciavatti, Z. Yao, R. Mescall, H. Hu, V. Semenenko, Z. Fei, and H. Li, "Terahertz nanoimaging of graphene," ACS Photonics **5**, 2645–2651 (2018).
[24] H. T. Stinson, A. Sternbach, O. Najera, R. Jing, A. S. Mcleod, T. V. Slusar, A. Mueller, L. Anderegg, H. T. Kim, and M. Rozenberg, "Imaging the nanoscale phase separation in vanadium dioxide thin films at terahertz frequencies," Nat. Commun. **9**, 3604 (2018).
[25] C. Maissen, S. Chen, E. Nikulina, A. Govyadinov, and R. Hillenbrand, "Probes for ultrasensitive THz nanoscopy," ACS Photonics **6**(5), 1279–1288 (2019).
[26] M. S. Vitiello, G. Scalari, B. S. Williams, and P. De Natale, "Quantum cascade lasers: 20 years of challenges," Opt. Express **23**, 5167–5182 (2015).
[27] P. J. de Groot *et al.*, "Ranging and velocimetry signal generation in a backscatter-modulated laser diode," Appl. Opt. **27**, 4475–4480 (1988).
[28] G. Plantier, N. Servagent, T. Bosch, and A. Sourice, "Real-time tracking of time-varying velocity using a self-mixing laser diode," IEEE Trans. Instrum. Meas. **53**, 109 (2014).
[29] G. Giuliani and S. Donati, "Laser interferometry," in *Unlocking Dynamical Diversity* (John Wiley & Sons, Ltd., 2005), pp. 217–255.
[30] S. Donati, "Self-mixing interferometry: A novel yardstick for mechanical metrology," Proc. SPIE **10150**, 101501I (2016).
[31] M. Brambilla, L. L. Columbo, M. Dabbicco, F. De Lucia, F. P. Mezzapesa, and G. Scamarcio, "Versatile multimodality imaging system based on detectorless and scanless optical feedback interferometry—A retrospective overview for a prospective vision," Sensors **20**, 5930 (2020).
[32] C. G. Derntl, G. Scalari, D. Bachmann, M. Beck, J. Faist, K. Unterrainer, and J. Darmo, "Gain dynamics in a heterogeneous terahertz quantum cascade laser," Appl. Phys. Lett. **113**, 181102 (2018).
[33] K. Otsuka, "Self-mixing thin-slice solid-state laser metrology," Sensors **11**, 2195–2245 (2011).
[34] A. D. Rakić *et al.*, "Sensing and imaging using laser feedback interferometry with quantum cascade lasers," Appl. Phys. Rev. **6**, 021320 (2019).
[35] P. Dean *et al.*, "Terahertz imaging through self-mixing in a quantum cascade laser," Opt. Lett. **36**, 2587 (2011).
[36] P. Dean *et al.*, "Coherent three-dimensional terahertz imaging through self-mixing in a quantum cascade laser," Appl. Phys. Lett. **103**, 181112 (2013).
[37] F. P. Mezzapesa, L. L. Columbo, M. Brambilla, M. Dabbicco, M. S. Vitiello, and G. Scamarcio, "Imaging of free carriers in semiconductors via optical feedback in terahertz quantum cascade lasers," Appl. Phys. Lett. **104**, 041112 (2014).
[38] M. Wienold, M. Wienold, T. Hagelschuer, N. Rothbart, L. Schrottke, K. Biermann, H. T. Grahn, and H. W. Hübers, "Real-time terahertz imaging through self-mixing in a quantum-cascade laser," Appl. Phys. Lett. **109**, 011102 (2016).
[39] R. Lang and K. Kobayashi, "External optical feedback effects on semiconductor injection laser properties," IEEE J. Quantum Electron. **16**, 347–355 (1980).
[40] F. P. Mezzapesa, L. L. Columbo, M. Brambilla, M. Dabbicco, S. Borri, M. S. Vitiello, H. E. Beere, D. A. Ritchie, and G. Scamarcio, "Intrinsic stability of quantum cascade lasers against optical feedback," Opt. Express **21**, 13748 (2013).

[41] S. Mastel, M. B. Lundeberg, P. Alonso-González, Y. Gao, K. Watanabe, T. Taniguchi, J. Hone, F. H. L. Koppens, and R. Hillenbrand, "Terahertz nanofocusing with cantilevered terahertz-resonant antenna tips," Nano Lett. **17**, 6526–6533 (2017).
[42] S. Mastel, A. A. Govyadinov, C. Maissen, A. Chuvilin, A. Berger, and R. Hillenbrand, "Understanding the image contrast of material boundaries in IR nanoscopy reaching 5 nm spatial resolution," ACS Photonics **5**, 3372–3378 (2018).
[43] J. Keeley *et al.*, "Measurement of the emission spectrum of a semiconductor laser using laser-feedback interferometry," Sci. Rep. **7**, 7236 (2017).
[44] F. Mooshammer, M. A. Huber, F. Sandner, M. Plankl, M. Zizlsperger, and R. Huber, "Quantifying nanoscale electromagnetic fields in near-field microscopy by Fourier demodulation analysis," ACS Photonics **7**, 344–351 (2020).
[45] T. Kalkbrenner, M. Graf, C. Durkan, J. Mlynek, and V. Sandoghdar, "High-contrast topography-free sample for near-field optical microscopy," Appl. Phys. Lett. **76**, 1206 (2000).
[46] M. S. Vitiello, L. Consolino, S. Bartalini, A. Taschin, A. Tredicucci, M. Inguscio, and P. De Natale, "Quantum limited frequency fluctuations in a terahertz laser," Nat. Photonics **6**, 525–528 (2012).
[47] X. Qi, G. Agnew, T. Taimre, S. Han, Y. L. Lim, K. Bertling, A. Demić, P. Dean, D. Indjin, and A. D. Rakić, "Laser feedback interferometry in multi-mode terahertz quantum cascade lasers," Opt. Express **28**, 14246 (2020).
[48] A. A. Govyadinov, I. Amenabar, F. Huth, P. Scott Carney, and R. Hillenbrand, "Quantitative measurement of local infrared absorption and dielectric function with tip-enhanced near-field microscopy," J. Phys. Chem. Lett. **4**, 1526–1531 (2013).
[49] A. Cvitkovic, N. Ocelic, and R. Hillenbrand, "Analytical model for quantitative prediction of material contrasts in scattering-type near-field optical microscopy," Opt. Express **15**, 8550–8565 (2007).
[50] R. Esteban, R. Vogelgesang, and K. Kern, "Tip-substrate interaction in optical near-field microscopy," Phys. Rev. B **75**, 195410 (2007).
[51] M. Brehm, A. Schliesser, F. Čajko, I. Tsukerman, and F. Keilmann, "Antenna-mediated back-scattering efficiency in infrared near-field microscopy," Opt. Express **16**, 11203–11215 (2008).
[52] A. S. McLeod, P. Kelly, M. D. Goldflam, Z. Gainsforth, A. J. Westphal, G. Dominguez, M. H. Thiemens, M. M. Fogler, and D. N. Basov, "Model for quantitative tip-enhanced spectroscopy and the extraction of nanoscale-resolved optical constants," Phys. Rev. B **90**, 085136 (2014).
[53] A. Arcangeli *et al.*, "Gate-tunable spatial modulation of localized plasmon resonances," Nano Lett. **16**, 5688 (2016).
[54] E. A. A. Pogna, M. Asgari, V. Zannier, L. Sorba, L. Viti, and M. S. Vitiello, "Unveiling the detection dynamics of semiconductor nanowire photodetectors by terahertz near-field nanoscopy," Light: Sci. Appl. **9**, 189 (2020).
[55] X. Guo, K. Bertling, and A. D. Rakić, "Optical constants from scattering-type scanning near-field optical microscope," Appl. Phys. Lett. **118**, 041103 (2021).
[56] W. Richter and C. R. Becker, "A Raman and far-infrared investigation of phonons in the rhombohedral V_2–VI_3 compounds Bi_2Te_3, Bi_2Se_3, Sb_2Te_3 and $Bi_2(Te_{1-x}Se_x)_3$ $(0 < x < 1)$, $(Bi_{1-y}Sb_y)_2Te_3$ $(0 < y < 1)$," Phys. Status Solidi B **84**, 619–628 (1977).
[57] V. E. Babicheva, "Long-range propagation of plasmon and phonon polaritons in hyperbolic-metamaterial waveguides," J. Opt. **19**, 124013 (2017).
[58] J.-S. Wu, D. N. Basov, and M. M. Fogler, "Topological insulators are tunable waveguides for hyperbolic polaritons," Phys. Rev. B **92**, 205430 (2015).
[59] N. A. Aghamiri, F. Huth, A. J. Huber, A. Fali, R. Hillenbrand, and Y. Abate, "Hyperspectral time-domain terahertz nano-imaging," Opt. Express **27**, 24231–24242 (2019).
[60] M. Schnell, M. Goikoetxea, I. Amenabar, P. Scott Carney, and R. Hillenbrand, "Rapid infrared spectroscopic nanoimaging with nano-FTIR holography," ACS Photonics **7**, 2878–2885 (2020).
[61] K. S. Reichel, E. A. A. Pogna, S. Biasco, L. Viti, A. Di Gaspare, H. E. Beere, D. A. Ritchie, and M. S. Vitiello, "Self-mixing interferometry and near-field nanoscopy in quantum cascade random lasers at terahertz frequencies," Nanophotonics **10**, 1495–1503 (2021).